PNAS RESEARCH ARTICLE | IMMUNOLOGY AND INFLAMMATION OPEN ACCESS

A temporal and spatial atlas of adaptive immune responses in the lymph node following viral infection

Shaowen Jiang[a,b], Jahanara Freedman[a,c], Madhav Mantri[a,b], Viviana Maymi[d], Scott A. Leddon[d], Peter Schweitzer[a], Subash Bhandari[a,d], Chase Holdener[a,b], Ioannis Ntekas[a], Christopher Vollmers[e], Andrew I. Flyak[d], Deborah J. Fowell[d], Brian D. Rudd[d], and Iwijn De Vlaminck[a,1]

Edited by Marc Jenkins, University of Minnesota Medical School, Minneapolis, MN; received March 3, 2025; accepted December 16, 2025

The spatial organization of adaptive immune cells within lymph nodes is critical for understanding immune responses during infection and disease. Here, we introduce AIR-SPACE, an integrative approach that combines high-resolution spatial transcriptomics with paired, high-fidelity long-read sequencing of T and B cell receptors. This method enables the simultaneous analysis of cellular transcriptomes and adaptive immune receptor (AIR) repertoires within their native spatial context. We applied AIR-SPACE to mouse popliteal lymph nodes at five distinct time points after Vaccinia virus footpad infection and constructed a comprehensive map of the developing adaptive immune response. Our analysis revealed heterogeneous activation niches, characterized by Interferon-gamma (IFN-γ) production, during the early stages of infection. At later stages, we delineated subanatomical structures within the germinal center (GC) and observed evidence that antibody-producing plasma cells differentiate and exit the GC through the dark zone. Furthermore, by combining clonotype data with spatial lineage tracing, we demonstrate that B cell clones are shared among multiple GCs within the same lymph node, reinforcing the concept of a dynamic, interconnected network of GCs. Overall, our study demonstrates how AIR-SPACE can be used to gain insight into the spatial dynamics of infection responses within lymphoid organs.

adaptive immune receptors | spatial transcriptomics | germinal centers | clonal evolution | lymph node microenvironment

Significance

Lymph nodes are key sites of adaptive immune responses, yet how immune cells coordinate their activities in space and time remains poorly understood. We combined high-resolution spatial transcriptomics with long-read immune receptor sequencing to study the dynamics of immune cells within lymph nodes following viral infection. We uncovered interferon-gamma activation niches during early infection, found that B cells exit germinal centers (GCs) from the dark zone, and observed clonal sharing of B cells across multiple GCs. These findings display how advanced spatial transcriptomics analysis can inform vaccine design and immunotherapies.

The adaptive immune system, mediated primarily by T and B cells, is central to pathogen defense, immune regulation, and the establishment of long-term immunological memory (1). T and B cells recognize specific antigens via their respective adaptive immune receptors (AIRs), the T cell receptor (TCR) and B cell receptor (BCR). The vast diversity of these receptors arises through V(D)J recombination, junctional diversity, and, in the case of B cells, somatic hypermutation (2, 3). Secondary lymphoid organs serve as key sites where naïve T and B cells encounter antigens, become activated, and undergo clonal expansion and selection (4). Elucidating the spatial organization of these immune cells within lymphoid organs is critical for understanding the cellular interactions and dynamic processes that drive immune responses during infection and disease.

Lymph nodes (LNs) are highly organized structures that facilitate pathogen defense and the orchestration of adaptive immunity (5, 6). Following infection, LNs not only act as sites for activation of adaptive immune cells but also function as dynamic microenvironments where cellular interactions evolve over time and space. Despite their central role in immune responses, several key aspects of LN biology remain poorly understood: How do innate immune cells initiate and coordinate infection responses within the LN microenvironment (7)? What mechanisms and spatial dynamics govern early T cell activation (8)? How do germinal center (GC) B cells exit the GC and differentiate into antibody-secreting plasma cells (9–12)? And at what specific times and locations does class-switch recombination occur in GC B cells (13)? While imaging (14), computational modeling (9), and bulk or single-cell sequencing (10, 12) have yielded valuable insights, these questions have yet to be pursued with high-throughput, spatially resolved molecular analysis.

Recent advances in spatial transcriptomics (ST) enable the analysis of spatial cellular and molecular organization in tissues (15–17). However, most ST methods rely on short-read sequencing, which is insufficient to resolve full-length TCR and BCR sequences. Several approaches have been proposed to overcome this limitation. Spatial VDJ (18) leverages the Visium platform (55-μm spots with 100-μm center-to-center spacing) to map AIR transcripts in tissues using both long-read and PCR-based short-read sequencing. Slide-TCR-seq (19) builds off the higher spatial resolution of Slide-seq (10 μm pixel size) to spatially map TCR transcripts and transcriptomes. However, these methods are limited in resolving AIR clonotypes at high single-cell resolution or detecting BCRs and TCRs concurrently.

Author affiliations: [a]Meinig School of Biomedical Engineering, Cornell University, Ithaca, NY 14853; [b]Department of Computational Biology, Cornell University, Ithaca, NY 14853; [c]Department of Biophysics, Cornell University, Ithaca, NY 14853; [d]Department of Microbiology and Immunology, Cornell University, Ithaca, NY 14853; and [e]Department of Biomolecular Engineering, University of California, Santa Cruz, CA 95064

Author contributions: S.J., M.M., B.D.R., and I.D.V. designed research; S.J., J.F., M.M., V.M., S.A.L., P.S., and S.B. performed research; S.J., C.H., I.N., and C.V. contributed new reagents/analytic tools; S.J. and J.F. analyzed data; I.N., A.I.F., and D.J.F. provided advice; and S.J., J.F., A.I.F., D.J.F., B.D.R., and I.D.V. wrote the paper.

The authors declare no competing interest.

This article is a PNAS Direct Submission.

[1]To whom correspondence may be addressed. Email: vlaminck@cornell.edu.

This article contains supporting information online at https://www.pnas.org/lookup/suppl/doi:10.1073/pnas.2504742123/-/DCSupplemental.

Published January 26, 2026.

Additionally, these approaches have been applied at a single time point, offering only a snapshot of immune cells in one organ.

To address these challenges, we developed AIR-SPACE, a methodology that combines high-resolution spatial transcriptomics with error-corrected, paired, full-length immune receptor sequencing. By applying AIR-SPACE to draining popliteal lymph node (PLN) samples collected at five timepoints following footpad injection with recombinant Vaccinia virus (VACV-gB) (20), we constructed a spatially resolved molecular atlas of LN immune responses throughout the course of infection. The data revealed the emergence of spatial niches associated with early LN responses, spatial and molecular evidence that plasma cells exit GCs via the dark zone–medulla interface, and evidence for B cell clonal recirculation between GCs. Collectively, these results underscore the potential of AIR-SPACE for dissecting complex immunological processes within lymphoid organs.

Results

High-Resolution Spatial Mapping of Immune Repertoires via AIR-SPACE. We designed and implemented AIR-SPACE, a spatial sequencing approach for simultaneous characterization of transcriptomes and AIR repertoires with high spatial and sequence resolution (Fig. 1). This assay offers: i) High spatial resolution (10 μm), ii) high sequence resolution, allowing recovery of long-read and paired receptor sequences for both B and T cells with low base-calling error rate, and iii) unbiased spatial transcriptomics of the same tissue. This is achieved by integrating high-resolution spatial transcriptomics with long-read, error-corrected AIR sequencing (*Materials and Methods*).

The AIR-SPACE protocol begins with a 10-μm tissue section mounted onto a spatial transcriptomics array (Curio Seeker, *Materials and Methods*). After RNA hybridization, reverse transcription, tissue clearing, second-strand synthesis, and complementary DNA (cDNA) amplification, the resulting cDNA library is split into two portions (Fig. 1*A*). One portion is reserved for short-read sequencing (Illumina), and the other portion is reserved for long-read sequencing of TCR and BCR transcripts (Fig. 1*A* and *Materials and Methods*). To specifically enrich BCR and TCR transcripts while retaining spatial barcodes, UMIs, and full-length cDNA, we used hybridization capture with probes tiling the constant region (Dataset S1). For long-read sequencing, we combined Oxford Nanopore Technology (ONT) with rolling circle to concatemeric consensus amplification (R2C2) (21) to achieve high-fidelity, full-length sequences, enabling precise characterization of the adaptive immune repertoire.

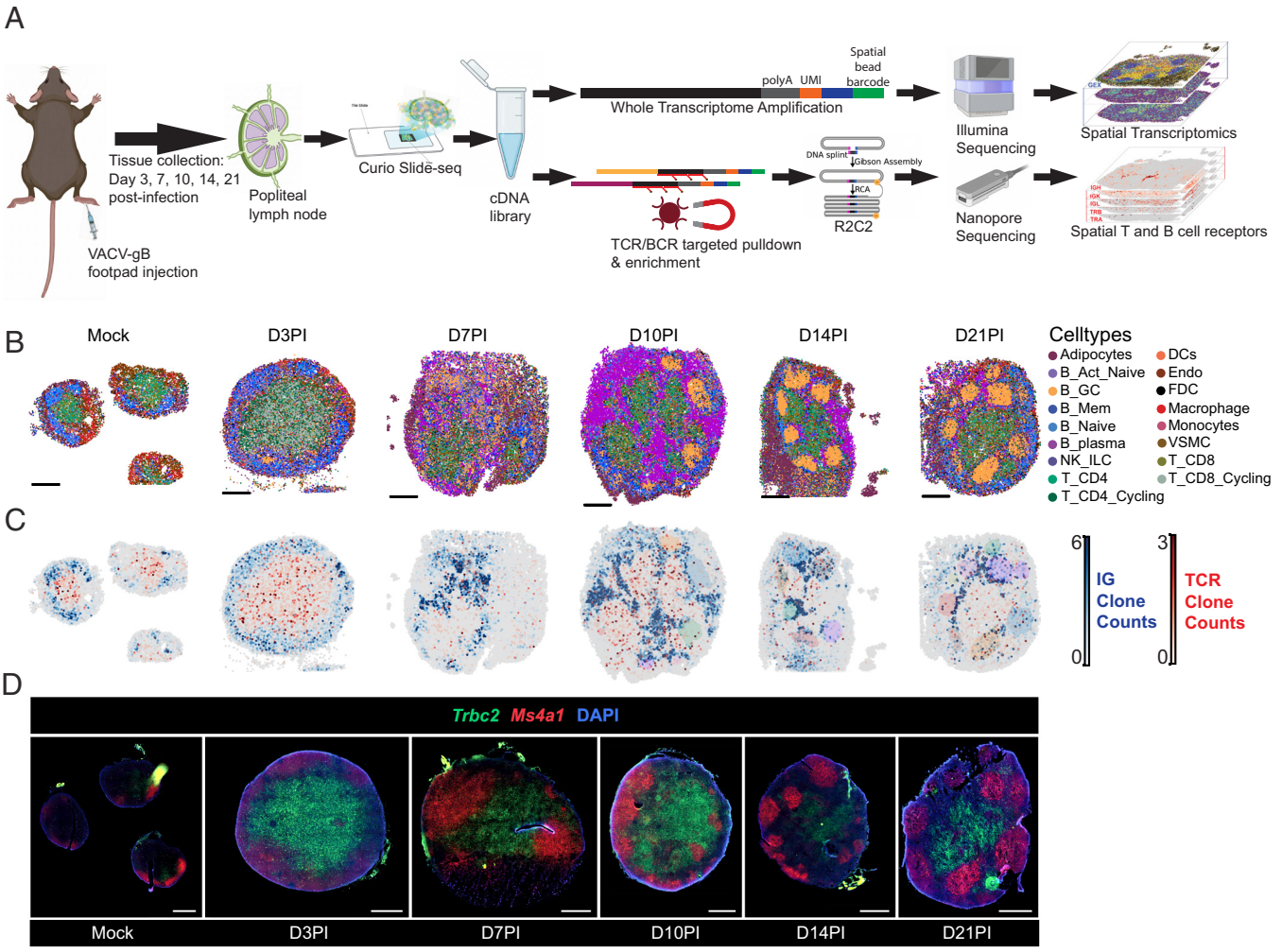

Fig. 1. AIR-SPACE enables the mapping of adaptive immune receptor (AIR) clonotypes and transcriptomics in situ. (*A*) Schematic of the experimental design and methodology, including the generation of long-read (LR) and short-read (SR). (*B*) Spatial mapping of cell types across the LN sections at different time points postinfection. (Scale bar, 500 μm.) (*C*) Spatial mapping of AIR clonotypes across the LN sections, with immunoglobulin (IG) clones shown in blue and T cell receptor (TCR) clones shown in red; outlined with germinal center (GC) regions in LNs from D10PI to D21PI. (*D*) Multiplexed RNA FISH staining for T cell marker *Trbc2* (green), B cell marker *Ms4a1* (red), and DAPI (blue) across all samples on sister sections. (Scale bar 500 μm.)

We employed this assay to study the temporal response of the LN to footpad injection with VACV-gB (*Materials and Methods*). We analyzed mouse PLN tissues at days 3, 7, 10, 14, and 21 postinfection (DPI). In addition, we analyzed mock controls collected at day 3 postinjection with PBS (Fig. 1*A* and *Materials and Methods*). Spatial transcriptomic sequencing enabled us to resolve the spatial structure of the LN by assigning cell types to beads using a deconvolution method with a combined lymphoid organ single-cell RNA sequencing (scRNA-seq) datasets (22–24) as a reference (*Materials and Methods*). Furthermore, by applying GraphST (25) to bead-level ST data for spatial domain detection, we identified and annotated spatially distinct regions of the LN, including the medulla, outer and inner cortex, GCs, and interfollicular border areas (conduit) (*SI Appendix*, Fig. S1*A* and *Materials and Methods*).

The spatial arrangement of cell types in the LNs corresponded well with known anatomical organization and reflected the temporal remodeling associated with the infection response. Specifically, T cells were predominantly localized to the paracortex (inner cortex), B cells were concentrated in the outer cortex, and macrophages were primarily distributed within the medulla and capsule regions of the LN. These patterns align well with canonical compartmentalization of LN (Fig. 1*B*). Histology staining and HCR-FISH imaging (26) of sister sections using T cell (*Trbc2*) and B cell (*Ms4a1*) markers confirmed these spatial distributions (Fig. 1*D* and *SI Appendix*, Fig. S13 and *Extended Materials and Methods*). Over the time postinfection, cycling T cells significantly increased in D3PI compared to Mock, while GC B cells and plasma cells emerged at later timepoints (D10PI, D14PI, D21PI). Notably, we observed nonrandom organization of CD4 and CD8 T cells within the paracortex, with CD8 T cells more centrally located and CD4 T cells predominantly at the periphery, which could facilitate effective antigen-specific T cell activation and coordination of adaptive immune responses (8) (*SI Appendix*, Fig. S1*B*). We validated cell type assignments by examining the expression of canonical marker genes (*SI Appendix*, Fig. S1*C*). While the canonical plasma cell transcription factor *Prdm1* (encoding BLIMP1) showed overall low expression across our dataset, when it was detected, it was enriched in plasma cells (*SI Appendix*, Fig. S18), consistent with its known role in plasma cell differentiation. To confirm the cell type dynamics captured in the spatial data, we performed fluorescence-activated cell sorting (FACS) analyses on multiple PLNs collected concurrently with those used for spatial transcriptomics. The composition of cell types measured by FACS closely mirrored trends observed in the spatial data. For example, plasma cells expanded rapidly between days 7 and 10 before declining, while T cells exhibited a sharp increase from day 3 to day 7, followed by a gradual decrease at later time points (*SI Appendix*, Fig. S1 *D* and *E*). Additionally, other cell types, including endothelial cells (Endo), dendritic cells (DCs), and follicular dendritic cells (FDCs) were observed in their expected regions within the LN section (*SI Appendix*, Fig. S1*F*).

AIR-SPACE Reveals the Temporal and Spatial Dynamics of AIR Repertoires Postinfection. To investigate the adaptive immune response following infection, we acquired an approximate total of 32 million reads by nanopore sequencing, with an average of 3 million reads per sample (*SI Appendix*, Fig. S2*A* and Table S1). We obtained high-fidelity consensus reads from the R2C2 reads using C3POa and BC1 (27). The consensus reads were demultiplexed from their putative barcode and UMI sequences, which were extracted from their relative positions anchored by the Curio adapter sequence. This process yielded a total of 990,767 consensus demultiplexed unique reads matching the bead-barcode whitelist, averaging 165,128 reads per sample. We assessed the fidelity of the reads by evaluating the constant region mapping identity score of immune repertoire sequences using IgBlast (28). This analysis revealed a median accuracy of 99.7% in the final processed reads (Fig. 2*A*). We also performed additional nanopore sequencing experiment on excess R2C2 pull-down libraries for D14PI and D21PI samples to increase sequencing depth. We collected approximately 3 million additional reads for each sample and 226,541 additional consensus demultiplexed unique reads.

For clonotype annotation of the TCR and BCR transcripts, we used MiXCR (29) to annotate the V(D)J regions and identify clonotypes within our dataset. The clonotype calling was defined by complementarity-determining region 3 (CDR3) sequences sharing the same V and J gene segments while allowing one mismatch or indel within the N-junctional diversity of CDR3 (*Materials and Methods*). This analysis identified a total of 6,045 IGH clones, 6,799 IGK clones, 359 IGL clones, 5,287 TRB clones and 1,291 TRA clones (Fig. 2*B*). After demultiplexing and clonotype calling, we mapped the AIR spatially from the long-read data, confirming that BCR-annotated reads predominantly localized to B cells, and TCR-annotated reads were mainly assigned to T cells (Fig. 1*C* and *SI Appendix*, Fig. S2*E*). We observed a strong correlation between short-read and long-read data for each AIR, supporting the robustness of our approach (*SI Appendix*, Fig. S2*D*).

To assess the spatial resolution achieved by AIR-SPACE for AIR clonotype calling, we examined the clonotype content of individual beads. We found that most beads with annotated clonotype contained a single clonotype sequence across all time points, with slight variations observed between receptor types (Fig. 2*C*). Overall, 83.7% of beads with annotated clonotype contained a single clonotype, including 82.1% of beads with IGH CDR3 sequences and 87.9% of beads with TRB CDR3 sequences, indicating that AIR-SPACE achieves near single-cell resolution in AIR annotation for most beads. This aligns well with previous observations from Slide-TCR-seq (19).

BCRs or antibodies comprise heavy and light chains, whereas TCRs comprise beta and alpha chains. Because paired BCR and TCR sequences determine antigen binding, experimental and computational methods have been developed to identify paired chains within individual B and T cells (30, 31). Using AIR-SPACE, we identified a total of 7,412 beads with paired IG heavy and light chain CDR3 sequences. These paired beads represented an average of 64.5% of all beads containing heavy chain CDR3 across all samples (Fig. 2*D*). Among these paired beads, an average of 34% had unique heavy-light chain CDR3 sequence combinations (Shannon entropy value of 0). For those beads without unique combinations, we observed that they are enriched in the conduit region of the LN, likely because of the high density of plasma cells packed in these regions (Fig. 2*E* and *SI Appendix*, Fig. S4*B*).

We explored whether differences in sequencing depth or cell type composition biased recovery of B cell receptor sequences. Antibody-secreting cells (ASCs) contributed more IGH molecules than GC B cells, consistent with their higher transcriptional output. However, this enrichment did not preclude robust GC clonal diversity analysis. Our additional long-read sequencing of D14PI and D21PI libraries increased total depth by ~1.8× to 1.9× and yielded ~1.4× to 1.7× more unique IGH molecules across both GC and ASC regions. Rarefaction analysis confirmed proportional recovery of unique molecules and clones with increasing depth and, specifically at the clone level, GC and ASC richness were comparable (*SI Appendix*, Fig. S12 and *Extended Materials and Methods*). These data indicate that deeper sequencing improves both GC and ASC sampling and that GC repertoires are well represented in our dataset.

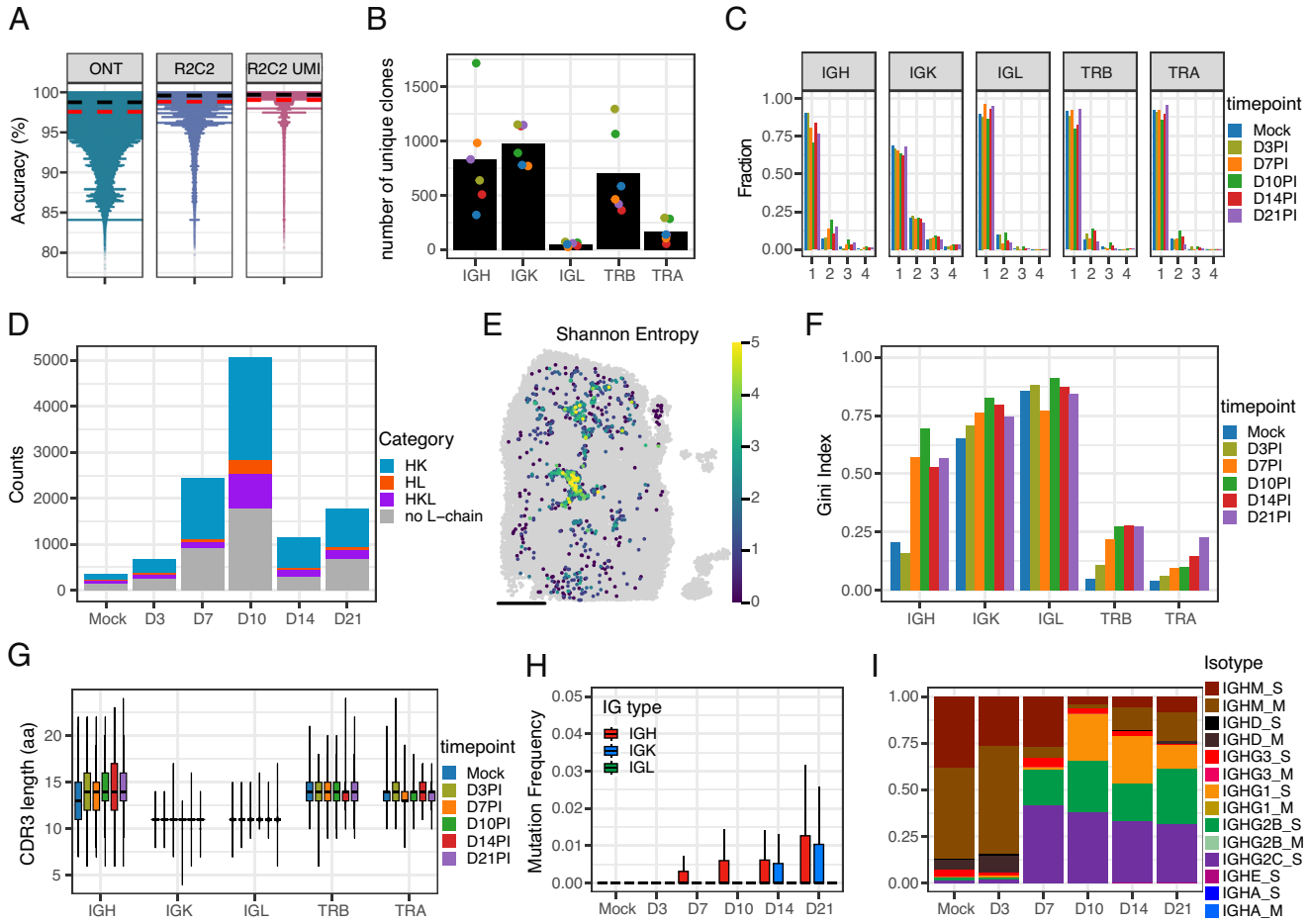

Fig. 2. Comprehensive analysis of AIR profiles from long-read sequencing. (*A*) Swarm plots comparing the accuracy of ONT reads postbasecalling (ONT), following R2C2 processing (R2C2), and after UMI correction and barcode sequences were mapped to the Curio barcode whitelist (R2C2-UMI overlap). (*B*) Barplot displaying the average number of unique clones identified for each receptor type (IGH, IGK, IGL, TRB, TRA) from LRs (R2C2-UMI overlap), with individual sample values represented by dots. (*C*) The fraction of beads containing a single or multiple clonotype sequence for each receptor type across samples. (*D*) Barplot showing the number of beads with detected heavy chains, categorized by the presence of paired IG receptors (HK: IGH and IGK; HL: IGH and IGL; HKL: IGH and IGK&L; no L-chain: no light chains were detected). (*E*) Spatial mapping of Shannon entropy index on LN of D14PI, calculated by potential combinations between heavy and light chains. (Scale bar, 500 μm.) (*F*) The Gini index represents the diversity of clonotypes for each receptor type across samples. (*G*) Boxplot showing the CDR3 length (aa) for each receptor across samples. (*H*) Boxplot showing the mutation frequency among IG receptors across samples. (*I*) Bar charts show the bulk composition of IGH chain isotypes across samples, with M as the membrane-bound BCR and S as the secreted antibody.

LNs serve as essential secondary lymphoid organs where the initiation and regulation of adaptive immune responses take place (4–6). We assessed the dynamic temporal changes in the AIR repertoire in the LNs as a function of time postinfection. First, we estimated the diversity of the repertoire using the Gini index, where a value of 1 represents maximal inequality among values. We observed decreasing diversity (increasing Gini index) as a function of time postinfection for B cell receptors, consistent with ongoing GC selection for B cells. A similar trend was observed for TCR (Fig. 2*F*). Notably, the diversity for the IG light chain repertoires (IGK, IGL) was consistently lower compared to the heavy chain. Additionally, we observed a greater number of shared light chain clonotypes across samples compared to heavy chains (IGH: 2, IGK: 521, IGL: 58). Both of these observations potentially reflect a higher level of coherence among light chains, consistent with previous findings of promiscuous light chains (30).

For each demultiplexed consensus read that could be clonotype-annotated, we measured CDR3 length and mutation frequency relative to the corresponding germline V(D)J gene (Fig. 2*G*). We also annotated IGH chain isotypes and determined whether they are membrane-bound (BCR) or secreted (antibody). B cells undergo two key processes in LNs: somatic hypermutation, which introduces somatic mutations in the variable regions, and class-switch recombination, which changes the isotype of produced antibodies (32). Both are mediated by the enzyme activation-induced cytidine deaminase (AID), encoded by the gene *Aicda*. The AIR-SPACE dataset captured expected temporal dynamics within the IG repertoires (IGH, IGK, IGL). IGH CDR3 length progressively increased over time (Fig. 2*G*), and mutation frequencies exhibited a gradual rise over time for both IGH and IGK (Fig. 2*H*). In parallel, at the bulk level across all beads, IG isotype composition shifted from IgM/D at early timepoints (D3PI, Mock) to predominantly secreted IgG antibodies from D7PI to D21PI. Notably, we observed an increased proportion of IgM/D isotypes and a decreased proportion of IgG3/1 at D14PI and D21PI, suggesting the potential recirculation of naive B cells or the egress of antibody-secreting plasma cells from the lymph node. (Fig. 2*I*).

Next, we examined whether AIR-SPACE could dissect cellular heterogeneity at the individual bead level. We integrated spatial region annotations with IGH-clonotype information and bead-level features (*Aicda* expression, IGH mutation frequency, isotype class, membrane/secreted isoform, and CDR3 length) for each sample (Fig. 3 and *SI Appendix*, Fig. S7). This analysis revealed marked temporal and spatial variations in isotype distribution across the LNs. For example, beads with IgG isotypes

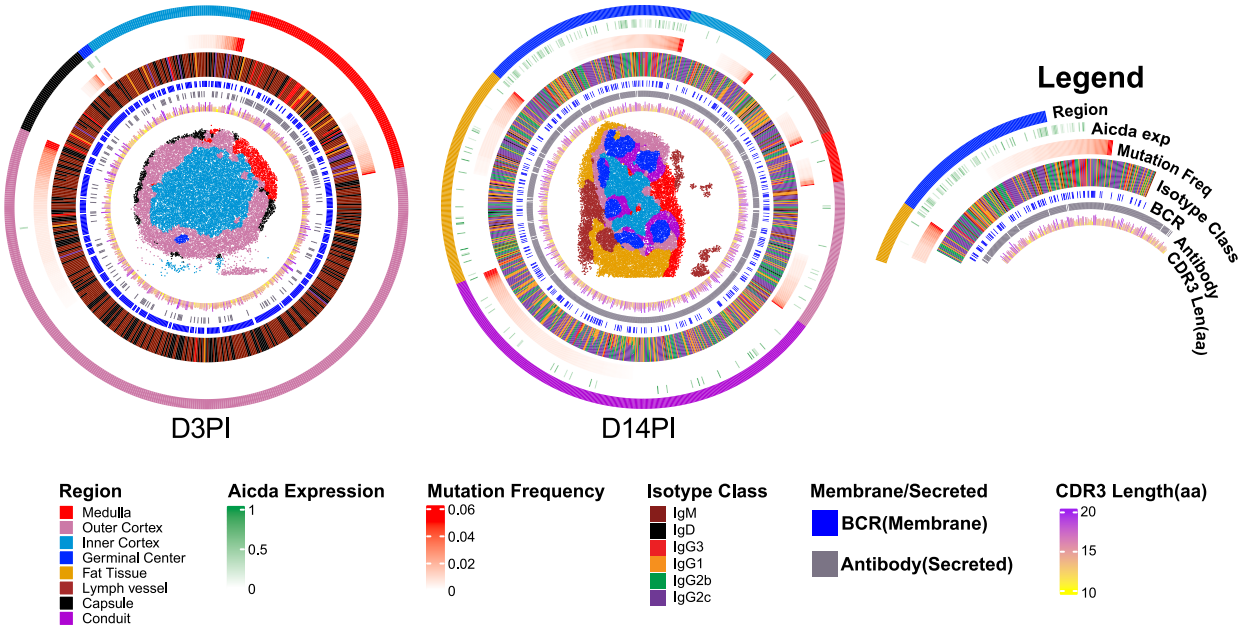

Fig. 3. Circos plots of individual beads with IGH clonotype sequences. Shown are representative sections at D3PI and D14PI, with a schematic track legend at *Right*. The central disk showing the spatial mapping of regions for each sample; Concentric rings display individual bead prosperities radiating outward: region annotation, *Aicda* expression, IGH mutation frequency, isotype class, BCR (membrane) or antibody (secreted) isoform, and CDR3 length (amino acids).

(IgG3/1/2b/2c) were predominantly localized to the medulla region in both Mock (91%, 2.5-fold enrichment) and D3PI (58%, 3.2-fold enrichment) samples, consistent with known anatomical localization of antibody-secreting cells in the LN medullary cords. Interestingly, at D14PI and D21PI, beads with IgM/D isotypes were primarily found in the outer cortex (D14PI: 25%, 2.1-fold enrichment; D21PI: 34%, 2.3-fold enrichment), suggesting the infiltration or recirculation of naïve B cells into follicular regions (*SI Appendix*, Fig. S8*A*). As anticipated, the beads in GCs showed significantly higher expression of *Aicda* at later time points (D14PI: 4.3 fold-change; D21PI: 5.3 fold-change) than other regions (*SI Appendix*, Fig. S8*B*). Analysis of highly mutated IGH bead (mutation rate > 0.01) revealed regional enrichment patterns, with the conduit region showing the highest proportion of highly mutated beads at D10PI (64.7%), which decreased at later time-points as mutations accumulated in GC (*SI Appendix*, Fig. S8*C*). Additionally, we also observed that beads with multiple isotypes were mostly distributed in conduit and medulla regions at later timepoints postinfection (D10-D21PI), indicating dense packing of plasma cells in these anatomical compartments (*SI Appendix*, Fig. S8*D*). Overall, AIR-SPACE resolved fine-scale immunological heterogeneity and dynamic changes in immune cell populations over time.

Spatial Niches of Interferon-Gamma Activation in the LN Early Postinfection. Interferon-gamma (IFN-γ) is a type II interferon that plays an essential role in controlling viral infections by inhibiting viral replication and enhancing both innate and adaptive immune responses (33). We observed elevated *Ifng* expression at D3PI, followed by a rapid decline at later time points (Fig. 4*A* and *SI Appendix*, Fig. S5*A*). At D3PI, *Ifng* expression localized to distinct LN regions (Fig. 4*B*). Using K-means clustering, we identified six *Ifng*-high clusters and categorized beads within a 200 μm radius of their centroids as "Inner niches" or "Outer niches," corresponding to their location in the inner or outer cortex, respectively. To establish appropriate controls, we identified regions with low *Ifng* expression in both the inner cortex (Control_in) and outer cortex (Control_out) of the D3PI and Mock samples, categorizing beads within a 200 μm radius of those centroids for comparison (Fig. 4*C* and *SI Appendix*, Fig. S5*B*). We then quantified *Ifng* expression as a function of distance from these niche centroids. Outer niches showed the highest overall *Ifng* expression, and both inner and outer niches exhibited a spatial gradient of decreasing *Ifng* levels with increasing distance from their centroids. In contrast, all control niches showed uniformly low *Ifng* expression at all distances (Fig. 4*D* and *Materials and Methods*).

To characterize the transcriptional modules associated with *Ifng*-rich areas, we performed spatial autocorrelation analysis (Fig. 4*E* and *SI Appendix*, *Extended Materials and Methods*). Gene set enrichment on positive *Ifng*-correlated genes (Pearson's r > 0.4, *SI Appendix*, *Extended Materials and Methods* and Dataset S2) revealed distinct pathway signatures for outer and inner niches. Outer niches showed enrichment of cytokine/chemokine signaling (*Cxcl10*, *Cxcl9*, *Ccl5*) and elevated cytotoxicity genes (*Gzma*, *Gzmb*) together with NK-associated receptors (*Klrb1b*/c, *Klrk1*) across distance-from-centroid profiles; We also observed higher *Trbc2* abundance in outer niches versus Control_out niches at both D3PI and Mock, consistent with increased T cell content (*SI Appendix*, Fig. S5*D*). Inner niches exhibited higher NF-κB signaling (*Nfkb1a*/b, *Ikbkb*), Th17 cell differentiation (*Irf4*, *Il1b*), and apoptotic processes (*Bcl2a1d*, *Bcl2a1b*, *Bcl2l1*, Fig. 4 *E* and *F* and *SI Appendix*, Fig. S5*E*). Moreover, TCR V-segment analyses showed that TRBV13-3 and TRBV4 usage, known to respond to injected pathogen VACV-gB (20), increased monotonically with proximity to the centroid in both Inner and Outer niches. By contrast, Control_in niche displayed comparable overall frequencies of these segments but lacked any distance-dependent gradient, and Control_out remained flat (Fig. 4 *G* and *H*).

Finally, we asked whether viral burden correlates with *Ifng* expression. Here, we examined VACV transcripts in the spatial transcriptomics data as a proxy for local antigen (*SI Appendix*, *Extended Materials and Methods*). Notably, VACV transcripts were only detected at D3PI from spatial transcriptomics data and localized primarily to the capsule and medulla regions (*SI Appendix*, Fig. S6). This pattern provides a mechanistic rationale for the

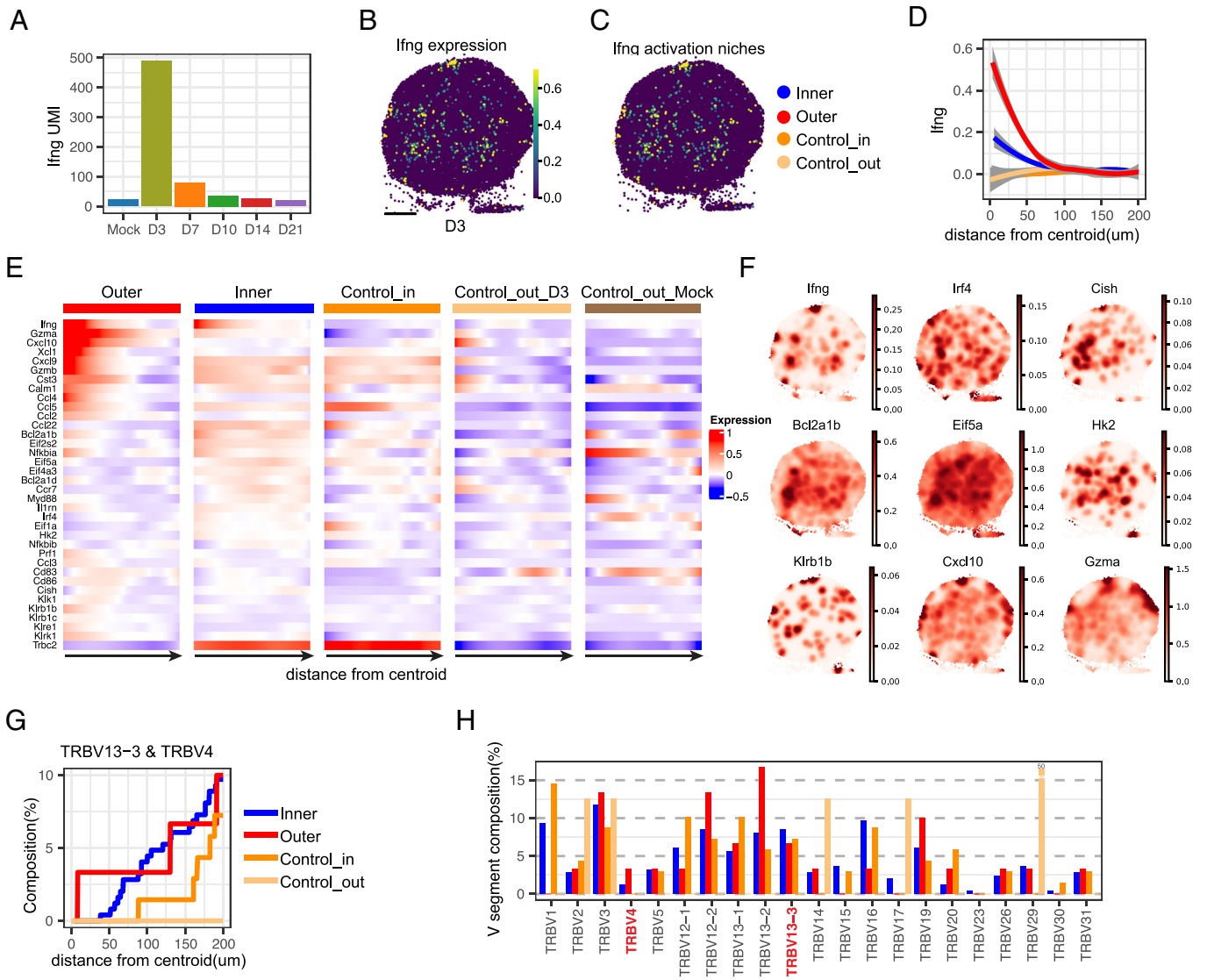

Fig. 4. Niches of activation from the expression on *Ifng*. (*A*) Total *Ifng* UMI counts aggregated across all samples. (*B*) Spatial expression of *Ifng* in D3PI LN. (*C*) Identification of *Ifng* activation niches in D3PI, categorized as inner (blue), Outer (red), Control_in (orange), and Control_out (light orange), corresponding to niches in the inner cortex, outer cortex, and control areas with low expression of *Ifng* in the inner or outer cortex, respectively. (*D*) *Ifng* expression levels as a function of distance away from the centroid of the four groups of niches, the color was shared with panel *B*. (*E*) Heatmap showing the expression levels of significantly spatial autocorrelated genes as a function of distance away from the centroid of the niches. (*F*) Spatial map on examples of genes positively correlated with *Ifng* in Gaussian smoothing value. (*G*) Composition of TRBV13-3 and TRBV4 gene segments as a function of distance away from the centroid of niches among four groups. (*H*) Composition of TRBV gene segments in the four groups of niches (color scheme as in g).

D3PI-restricted *Ifng* signal: the absence of viral reads after D3PI is consistent with early control/clearance below our detection threshold, aligning with the subsequent decline in *Ifng* expression. Importantly, this spatial configuration is consistent with models in which afferent pathogens are captured by subcapsular sinus and medullary macrophages to stimulate rapid production of IFN-γ (34).

Taken together, these data indicate that early *Ifng* expression in the outer cortex is consistent with a combination of NK-cell and bystander/effector CD8 T cell activity, while inner cortex *Ifng*-high niches are more consistent with antigen-specific T cell responses.

AIR-SPACE Characterizes GC Compartments and B Cell Spatial Dynamics. GCs are specialized microanatomical sites in secondary lymphoid organs where B cells undergo clonal expansion and antibody affinity maturation (32). To investigate the spatial organization and dynamic evolution of B cells within GCs, we focused on samples from later time points when GCs are mature and well-developed (*SI Appendix*, Fig. S9*A*). We analyzed well-segregated GCs that exhibited clear microanatomical features (Fig. 5 *A* and *B* and *SI Appendix*, Fig. S10 *A* and *B*). Unsupervised clustering with GraphST (25) identified light and dark zones (LZ and DZ, *SI Appendix*, Fig. S9*B*). LZ markers (*Cxcl13* and *Cxcr5*) were more highly expressed in the LZ, with expression levels increasing progressively as beads were positioned farther from the LZ–DZ boundary. Conversely, DZ markers (*Cxcl12*, *Cxcr4*) formed corresponding spatial gradients (Fig. 5*C* and *SI Appendix*, Fig. S9*D*). These findings align with the well-established DZ/LZ molecular architecture, driven by chemokines (*Cxcl12*, *Cxcl13*) and their receptors (32) (*Cxcr4*, *Cxcr5*). Differential expression analysis further highlighted functional differences between LZ and DZ (*SI Appendix*, Fig. S9*C* and Dataset S5). *Aicda* ($P = 3.3e{-}07$) and G2M scores ($P < 2.22e{-}16$) were elevated in DZ, consistent with active clonal expansion and somatic hypermutation. *Bcl2a1b*

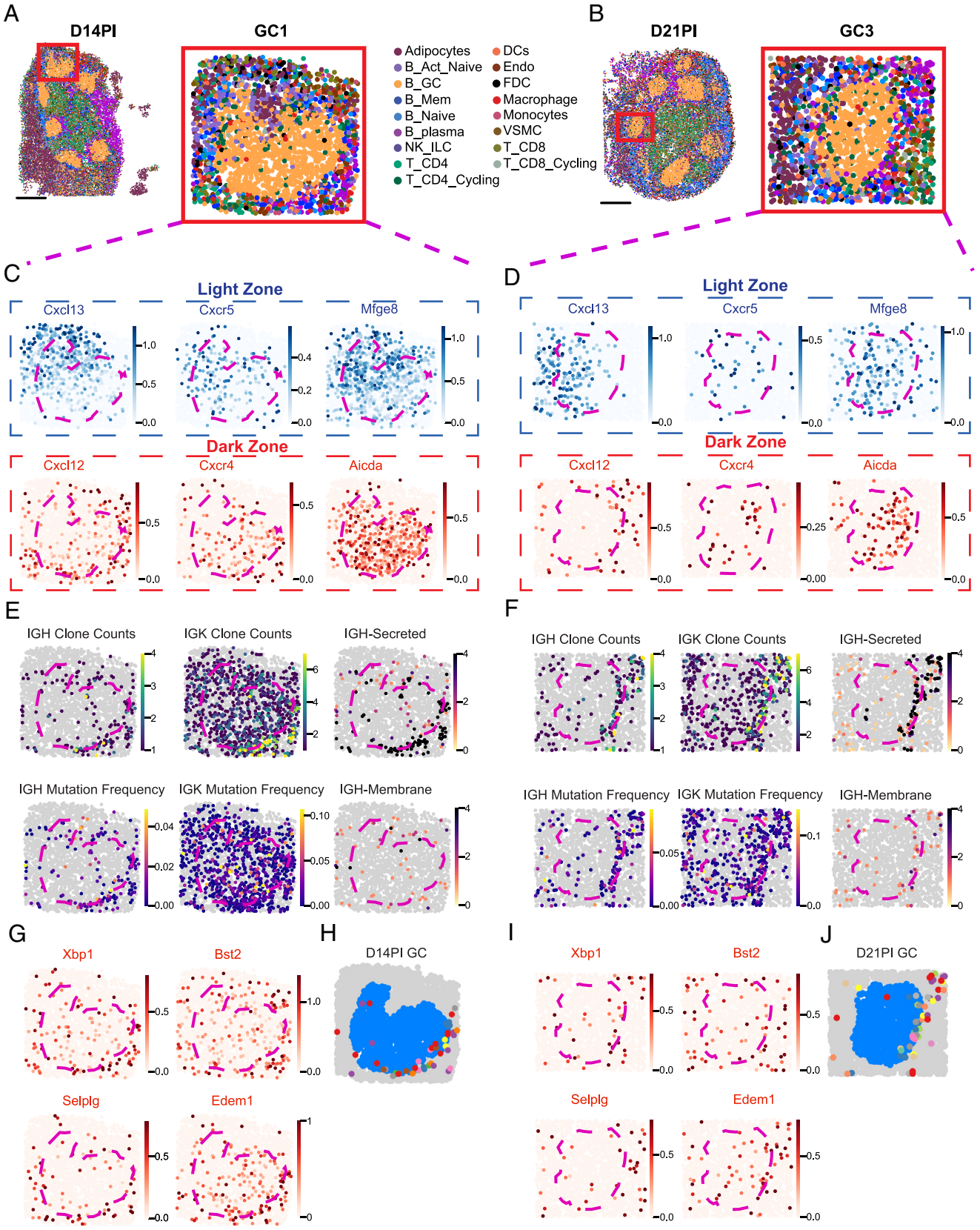

Fig. 5. AIR-SPACE uncovers GC egress zone in D14PI & D21PI. (*A* and *B*) Zoomed-in view of GCs (D14PI-GC1, D21PI-GC3) from D14PI and D21PI samples, colored by different cell types; Spatial mapping of cell types across the LN sections at different time points postinfection. (Scale bar, 500 μm.) (*C* and *D*) Spatial expression of LZ (*Cxcl13, Cxcr5, Mfge8*) and DZ (*Cxcl12, Cxcr4, Aicda*) marker genes. (*E* and *F*) Spatial mapping of adaptive immune repertoire information from LR. (*G* and *H*) Spatial expression of preplasma cell marker genes (*Xbp1, Bst2, Selplg, Edem1*) and spatial map of IGH clones on D14PI GC1, color-coded by different IGH clones. (*I* and *J*) Spatial expression of preplasma cell marker genes (*Xbp1*, *Bst2*, *Selplg*, *Edem1*) and spatial map of IGH clones on D21PI GC3, color-coded by different IGH clones.

(P = 0.0039) and the FDC marker *Mfge8* (35) (P = 3.8e–12) were higher in the LZ, suggesting antigen-driven selection. Application of this analysis to additional LN sections confirmed these patterns (Fig. 5*D* and *SI Appendix*, Fig. S10 *C* and *D*).

Notably, we identified numerous beads at the DZ–medulla interface displaying plasma cell–like features: high *Xbp1* expression, low *Aicda* expression, abundant IGH secreted isoforms, and elevated IGH mutation frequency (Fig. 5 *E* and *F* and *SI Appendix*, Fig. S10 *E* and *F*). By applying spatial autocorrelation analysis on these GCs and investigating gene expression highly correlated with IGH secretion processes (Dataset S3), we identified several putative preplasma cell markers (10), including *Bst2* and *Selplg* (Fig. 5 *G* and *I* and *SI Appendix*, Fig. S10 *G* and *I*). We also found genes associated with KEGG pathway database: "Protein processing in the endoplasmic reticulum" (*Mzb1*, *Edem1*), "N-Glycan biosynthesis" (*Man1b1*, *Ddost*), and "Antigen processing and presentation" (*H13*, *H2-Q7*) (*SI Appendix*, Fig. S9 *I* and *J*). These pathways are characterized as features of plasma cell differentiation due to their roles in supporting the production of high quantities of antibodies (36). Importantly, by spatial tracking identical IGH clones within the GC, we observed that these cells appear to migrate out of the GC via the DZ interface (Fig. 5 *H* and *J* and *SI Appendix*, Fig. S10 *H* and *J*). These findings support the theoretical model (9) that these cells are preplasma cells exiting the GC through the DZ after selection and differentiation. Additionally, DZ–medulla interface enrichment of *Xbp1*-high/*Aicda*-low beads, elevated IGH-S isoforms, and higher IGH mutation frequencies were likewise observed in two additional D14PI GCs, reinforcing the DZ-egress model (*SI Appendix*, Fig. S11). Collectively, these findings demonstrate the utility of AIR-SPACE to capture both the transcriptional differences and clonal dynamics of B cells, including the emergence and egress of preplasma cells, thereby providing insights into the spatial and temporal complexity of B cell–plasma cell differentiation within GCs.

Recent studies demonstrate that individual B cell clones can expand and undergo selection in multiple GCs, indicating B cell recirculation (14, 37). To investigate this phenomenon through the lens of AIR-SPACE, we performed the spatial lineage analysis and examined the spatial distribution of IGH clones across GCs. We first assigned each IGH clone (with at least five beads in the spatial data) to a GC by measuring the Euclidean distance between its bead coordinates and the identified GCs (*SI Appendix*, Fig. S9*A*). Beads within 100 μm were assigned to that GC. If multiple beads from the same clone were associated with different GCs, the clone was categorized as "Multiple GCs." Clones with all beads assigned to the same GC or with no GC assignment were categorized as "Single GC" or "non-GC" clones, respectively. Applying this classification to LNs with developed GCs (D10PI, D14PI, D21PI) showed that although most IGH clonal families were confined to a single GC, a notable fraction spanned multiple GCs (Fig. 6*A*). Interestingly, the proportion of "Multiple GCs" clones increased over time: 6.9% at D10PI, 17.5% at D14PI, and 22.9% at D21PI (Fig. 6*A*). The number of clones assigned to each GC ranged from 35 to 261, with a median of 86 clones per GC. To rule out potential edge effects, we varied the clone-to-GC assignment threshold from 80 to 120 μm (*SI Appendix*, Fig. S14). While absolute clone numbers increased with a larger threshold, the relative proportion and distribution pattern of multi-GC clones remained similar across all thresholds. In agreement with a previous study (37), the distribution of the number of shared IGH clones by the number of GCs fits well with a Poisson/Negative binomial distribution, indicating that the recirculation of a B cell to a different GC is a stochastic mechanism (Fig. 6*B*). Spatial mapping revealed inter-GC clones distributed across multiple GCs, with some clones detected just outside GC, potentially representing B cells transiting near egress zones, consistent with previous observations of preplasma cells exhibiting "random sprints" through LN compartments (38) (Fig. 6*C*). Taken together, these findings support the idea of recirculation of clones and inter-GC exchange as has been suggested previously (37).

Understanding how antibody affinity shapes plasma cell (PC) differentiation from GC B cell selection is an active area of research (39–41). Consistent with prior work (41), we found PC clones (IGH) displayed lower clonal diversity than contemporaneous GC clones (higher Gini indices), particularly at early timepoints postinfection (D7&10PI, Fig. 6*D*). To directly link GC B cells to GC-derived PCs within the same clonal lineage, we leveraged AIR-SPACE to identify shared abundant clones (with ≥5 spots containing both GC and PC from cell-type annotation) and compared their IGH mutation rates between GC and PC compartments. PC mutation rates (IGH) were significantly higher than GCs during early infection (D7&10PI), with the difference diminishing at later timepoints (Fig. 6 *E* and *F*). When examining the correlation between these PC and GC mutation rates for shared clones, we observed no correlation from D7PI to D14PI (R^2 < 0.05), but a positive correlation emerged by D21PI (R^2 = 0.149, P < 0.0001) (Fig. 6*F*). These observations align with recent findings by ElTanbouly et al. (41) in which progressive selection within the GC enriches the PC compartment for higher mutation over time. AIR-SPACE enables direct comparison of mutation rates within the same clonal lineages across spatial.

Finally, to explore sequence-level analysis of immune cell clonal evolution, we constructed phylogenetic trees for a subset of prominent IGH clonal families and investigated their lineage diversification and mutation accumulation as a function of location within the LN (*Materials and Methods*). One D14PI IGH clone (CDR3: CTTGGYGNYDYYAMDYW) stood out: The lineage tree of this clonal family revealed a branching structure indicative of ongoing somatic hypermutation and class switching recombination (Fig. 6*G*). Its variants were spatially distributed across 3 neighboring GCs, as well as regions not assigned to any GC in the outer cortex of the LN. Other IGH clones show more evenly spread distributions across the LN (*SI Appendix*, Fig. S15). These spatial patterns imply that B cells shuttle among multiple GCs as they undergo affinity maturation. Together, these data indicate that GCs are not isolated microenvironments. Instead, they appear to function as interconnected nodes in a dynamic network, allowing B cells to circulate among multiple GCs, potentially enhancing the efficiency and diversity of the affinity maturation process.

Discussion

In this study, we introduce AIR-SPACE, a method that integrates high-fidelity long-read sequencing of target-enriched AIR transcripts with unbiased spatial RNA sequencing. We used this method to construct an atlas of the temporal and spatial dynamics of immune repertoire changes in mouse popliteal lymph node (LN) tissues over the course of VACV-gB infection. The immune cell clonotypes measured in this way localized to their expected LN structures, and their temporal changes aligned with the established trajectory of the adaptive immune response. The data further provide additional insights into the spatiotemporal dynamics of the LN microenvironments following viral infection.

First, we examined mechanisms of T cell priming in the LN during the early response to infection. Previous work (42, 43) has shown that IFN-γ is essential for antiviral immunity in LNs. Both NK cells and bystander/memory CD8 T cells positioned near afferent lymphatics provide early production to enhance innate

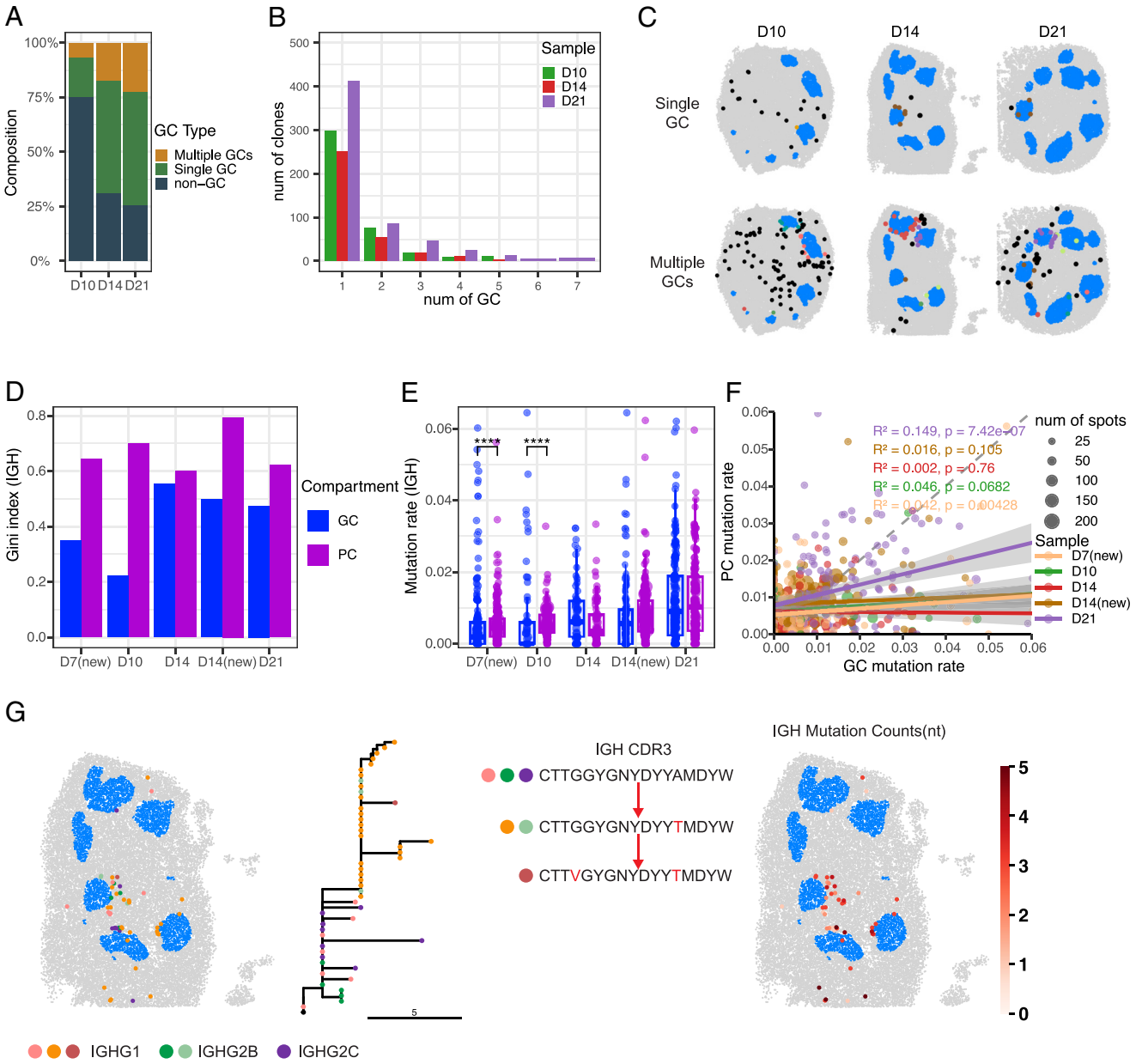

Fig. 6. AIR-SPACE uncovers inter-GC B cell recirculation and clonal evolution. (*A*) Percentage of IGH clones found in multiple GCs (brown), single GC (dark green), or non-GC (black) at different time points (D10PI, D14PI, and D21PI). (*B*) The distribution of the number of IGH clones by the number of GCs for each sample. (*C*) Spatial map showing examples of IGH clones shared across multiple GCs for different time points (D10PI, D14PI, and D21PI). *Top*: examples of single GC; *Bottom*: examples of multiple GCs. Blue dots represent individual GCs, black dots indicate beads not assigned to any GC, while colored dots correspond to beads assigned to adjacent GCs. (*D*) Gini index (IGH) for GC (blue) and PC (magenta) compartments across samples with GCs. Higher values indicate lower diversity. (*E*) IGH mutation rates in GC (blue) versus PC (magenta) compartments for shared clones. Boxplots show median and quartiles; statistical comparisons by the Wilcoxon rank-sum test (****$P < 0.0001$). (*F*) Correlation between GC (x-axis) and PC (y-axis) mutation rates for shared clones across samples. Each point represents one shared clone, sized by number of spots. Lines show weighted least-squares regression with 95% CI; the dashed line shows y = x. R^2 and *P*-value displayed for each sample. (*G*) Clonal evolution of a single IGH clone family from the D14PI sample. Spatial mapping and lineage tree represent each individual bead within the family, colored by different isoforms and CDR3 sequences. Branch lengths reflect the number of mutations (nt) accumulated from the germline (black node: root), and its spatial map.

responses, while virus-specific CD8 T cells sustain IFN-γ levels during the adaptive phase to suppress viral replication and prevent tissue damage. However, the reprogramming pathways of the IFN-γ activation and the spatial components within the microenvironment remain poorly defined. By mapping IFN-γ expression, we identified discrete activation niches in the early postinfection LN that exhibited heterogeneous gene expression profiles depending on LN location. Niches in the outer cortex were marked by strong innate immune signatures, including elevated cytotoxicity genes and NK-associated receptors and *Trbc2*, whereas niches in the inner cortex displayed gene expression patterns indicative of T cell activation, likely involving antigen-specific T cells as corroborated by in situ TCR clonotype data. Importantly, VACV transcripts were detected only from the same ST library (D3PI) and localized primarily to the subcapsular sinus and medullary regions. The location of viral antigen at these sites align with previous work showing virions can reach the draining LN within hours of infection, triggering rapid innate IFN-γ production and facilitate CD8 T cells priming by antigen-presenting cells (5, 7, 44). We anticipate that utilizing AIR-SPACE to study these very early timepoints will yield further perspectives into these mechanisms.

AIR-SPACE also enabled in-depth characterization of the spatial organization of GC microenvironments and B cell spatial dynamics within the LNs. Notably, we achieved a deeper understanding of the differentiation of GC B cells to plasma cells. Meyer-Hermann et al. (9) previously used computational modeling to study these differentiation dynamics and concluded that B cells likely leave the GC as plasma cells via the DZ rather than the LZ. Prior classical models (45, 46) assumed that GC B cells leave the GC directly via the LZ after selection. An additional model (9) found that after positive selection in the LZ, GC B cells migrate back to the DZ, where they undergo division and differentiate into plasma cells if their antigen was retained, and ultimately exit the GC via the DZ. This model is supported by imaging and mRNA microarray analysis (11, 12), which further highlights the role of T follicular helper cells in driving plasma cell egress from the DZ. Consistent with these studies (9–12), we identified a clear population of plasma cells around the DZ–medulla interface with high expression of *Bst2*, *Selplg*, and *Xbp1*, low expression of DZ B cell markers (*Aicda* and G2M proliferation score), and upregulation of endoplasmic reticulum and protein export–related genes. Furthermore, by analyzing the positioning of B cell clonotypes across the DZ–medulla interface, we observed a gradient increase at this interface in antibody expression and IGH mutation frequency—clear plasma cell features. Although our data offer only snapshots of this dynamic process, the distribution of identical IGH clones around the DZ–medulla interface provides valuable clues regarding the GC B-to-plasma cell egress pathway. Collectively, our observations provide molecular and genetic evidence that antibody-secreting plasma cells exit the GC via the DZ–medulla boundary.

A deeper understanding of the mechanisms governing the development and dynamics of B cell clones within and between GCs is crucial for vaccine design (14). Tas et al. (14) used multiphoton imaging and a multicolor confetti mouse system to reveal sharing of B cell clones between GCs within the same LN (14). Later, Pelissier et al. (37) used a combination of laser capture microdissection of individual GCs and repertoire sequencing to substantiate the evidence of B cell recirculation among GCs in LNs (37). By mapping B cell clonotypes spatially using AIR-SPACE, we likewise observed shared B cell clones across multiple GCs. Furthermore, AIR-SPACE allows direct comparison of GC and PC maturation within the same clonal lineage. Our data offer details by enabling spatial lineage tracing of a B cell clonal family within a single LN section via phylogenetic tree analysis, allowing us to better understand the heterogeneity of these dynamic processes not only among different GCs but also across various B cell clones. Applying AIR-SPACE to study antigen boosting may illuminate secondary responses that involve the formation and reactivation of memory B cell clones (47).

AIR-SPACE offers several advantages over previous spatial antigen receptor methods. First, a key advantage is its ability to characterize both T and B cell clonotypes in situ at high 10-μm spatial resolution, to resolve paired TCR/BCR sequences within the same spot. Second, AIR-SPACE is compatible with multiple commercially available platforms for spatial transcriptomics and does not require specialized equipment, making it easily adoptable. Several important limitations remain. AIR-SPACE achieves near single-cell rather than true single-cell resolution, which most significantly impacts the assessment of dense LN. In addition, the recovery rate of paired IG chain from AIR-SPACE is lower than commercial single-cell V(D)J assays. From our rarefaction analysis, we note an increase in captured IGH molecules and clones when we added our additional sequencing experiment for samples D14PI and D21PI. This indicates that further sequencing depth could still capture more unique clones and molecules and suggests that the diversity and counts captured in our study likely underestimates the total clonal complexity of our samples. These trade-offs between spatial resolution and capture/pairing efficiency are inherent to current spatial transcriptomics technologies but do not compromise our conclusions on clonal expansion, GC dynamics, or inter-GC connectivity.

Looking ahead, AIR-SPACE opens avenues for exploring adaptive immune responses in a variety of contexts, for example, investigation into immune responses to various pathogens (48, 49), autoimmune conditions (50), gut microbiome–immune relationships (51, 52), or tertiary lymphoid structures within cancers (53). Moreover, integrating AIR-SPACE with emerging spatial total transcriptome methods (52, 54) or spatial proteomics technology (55) could broaden the scope for studying systems immunology. As spatial sequencing technologies continue to evolve, enhancements in resolution, sensitivity, and scalability will likely expand the utility of AIR-SPACE, enabling more comprehensive insights into the cellular and molecular landscapes of immunity. Ultimately, the knowledge gained from such advancements has the potential to guide antibody design strategies and deepen our understanding of immune-mediated diseases.

Materials and Methods

Sample Information and Processing. Mature adult male mice (3-mo-old; C57BL/6J; male) were injected with 1e5 PFU Vaccinia virus (VACV-gB) in the left hind footpad via 30G needles. Equal volume of PBS was injected to the mice of the same age as controls. These virus-infected mice and controls across five different time points, namely D3 (infected and Mock), D7, D10, D14, D21, were used for spatial transcriptomics experiments. After isoflurane anesthesia, the left PLNs of these mice were extracted using an aseptic technique and were immediately embedded in cryomolds with O. C. T Compound (Tissue-Tek) media and fresh frozen directly on dry ice and stored at −80 °C.

Slide-Seq Spatial Transcriptomics Library Preparation and Sequencing. Slide-seq spatial transcriptomics experiment was performed using the Curio Seeker Kit (Curio Bioscience) according to manufacturer instructions. In brief, a 10-μm thickness tissue section from each collected fresh-frozen PLN was mounted on a 3-mm x 3-mm spatially indexed bead surface Curio Seeker tile. After RNA hybridization and reverse transcription, the tissue section was digested, and the beads were removed from the glass tile and resuspended. Second-strand synthesis was then performed by semirandom priming followed by cDNA amplification. A sequencing library was then prepared using the Nextera XT DNA sample preparation kit (Illumina). The library was sequenced on an Illumina NextSeq 2 K (Illumina) platform using a P3 100 bp kit, with reads allocated as follows: 50 bp for read 1, 8 bp for index 1, 8 bp for index 2, and 72 bp for read 2.

Hybridization-Based Target Enrichment of TCR and BCR Transcripts. Hybridization-based target enrichment of TCR and BCR transcripts was performed using the IDT xGen NGS target enrichment kit. BCR and TCR custom-designed 5′-biotinylated oligonucleotide panels were used separately for capture and pulldown of target molecules of interest. The BCR panel includes 151 probes consisting of *Igh, Igk, and Igl* gene loci, and the TCR panel includes 81 probes consisting of *Trb, Tra, Trg, and Trd* gene loci (Dataset S1). In order to have sufficient material, the input cDNA libraries were amplified prior to the hybridization reaction. We used 5 to 10 ng of Slide-seq cDNA per library. PCRs were performed using KAPA HiFi HotStart ReadyMix (2×) (Roche) with cDNA primers (10× Genomics). The total volume and number of PCR cycles of reaction varied depending on the original cDNA amount in each library. After PCR amplification, each library was performed bead wash with 0.6× SPRIselect and eluted in 40 μL of water. Next, we followed the protocol "xGen hybridization capture of DNA libraries" (version 7, IDT) with "Tube protocol" with slight modifications. Specifically, we separated the hybridization reaction for each sample into TCR and BCR individually, using 200 ng of PCR-amplified DNA as the input library for each. Postcapture PCR was performed for each pull-down library using KAPA HiFi HotStart PCR with

14 cycles, followed by two rounds of 0.6X SPRIselect as postcapture PCR clean-up and eluted in 22 μL H_2O.

Rolling Circle Amplification to Concatemeric Consensus (R2C2). We first generated the splint by using 23 μL of H_2O, 25 μL of KAPA HiFi HotStart ReadyMix (2×), 1 μL of UMI_Splint_Forward (100 μM) and 1 μL of UMI_Splint_Reverse (100 μM). The mix was incubated for 3 min at 95 °C, for 1 min at 98 °C, for 1 min at 62 °C and for 6 min at 72 °C. The DNA splint was then purified with the Select-a-size DNA Clean and Concentrator kit (Zymo Research) with 85 μL of 100% EtOH in 500 μL of DNA binding buffer. Next, 200 ng of target-enriched DNA was mixed with 200 ng of DNA splint and 10 μL NEBuilder HiFi DNA Assembly Master Mix (2×) (New England Biolabs, NEB) was added. The mix was incubated for 1 h at 50 °C. After incubation, each reaction was added 5 μL of NEBuffer 2, 3 μL of Exonuclease I, and 3 μL of Exonuclease III, and 3 μL of Lambda Exonuclease (all NEB), and adjusted the volume to 50 μL with H_2O. The mixture was then incubated for 6 h at 37 °C followed by a heat inactivation step for 20 min at 80 °C. The circulated DNA was then extracted using 0.8X SPRIselect and eluted in 40 μL H_2O. After purification, each circularized DNA was split into 4 aliquots of 10 μL. Each aliquot was amplified in its own 50 μL Rolling circle amplification reaction [formula as in R2C2 paper (21)] and incubated at 30 °C overnight. After incubation, 2 μL T7 Endonuclease was added to each reaction and then incubated for 2 h at 37 °C with occasional agitation. Cleanups with SPRI beads in 0.5x ratio of H_2O were performed to extract the debranched DNA and eluted in 40 μL H_2O.

Oxford Nanopore Long-Read Library Preparation and Sequencing. Each resulting DNA from R2C2 was sequenced using one separate ONT MinION (R10.4.1) flow cell. For each run, 1 to 2 μg of DNA was prepared using the Ligation Sequencing Kit V14 following the manufacturer's protocol as in "DNA repair and end-prep" and "Adapter ligation and clean-up". Each library was then loaded into the flow cell according to the protocol instructions. Each run lasted at least 48 h, and the sequencing results were stored in the state-of-art format.

Long-Read Data Preprocessing. After ONT long-read sequencing, each resulting data was base called using the superaccuracy model (SUP) of the GPU accelerated Guppy algorithm (v6.5.7, config file: dna_r10.4.1_e8.2_400bps_sup.cfg). Basecalled reads were then processed and demultiplexed into R2C2 consensus reads and their subreads using C3POa (v3) with corresponding splint sequences (Dataset S4). After that, BC1 commands were applied in the above reads to generate R2C2+UMI consensus reads(*27*). Next, R2C2+UMI reads were demultiplexed in a similar manner as BLAZE pipeline with modification. Specifically, we changed the following parameters in the config.py file from BLAZE[34] so that the pipeline can work for Slide-seq library structure [ADPT_SEQ = "TCTTCAGCGTTCCCGAGA;" PLY_T_LEN = 8; PLY_T_NT_AFT_ADPT = (13, 50); DEFAULT_UMI_SIZE = 7; DEFAULT_BC2_SIZE = 6; DEFAULT_BC1_SIZE = 8]. After anchoring the adaptor (linker) sequence with an allowance of one Levenshtein edit distance and identifying its position in each read, we extracted the putative barcode and UMI sequences based on their relative position from the adaptor. Next, the resulting reads that can be anchored to the Slide-seq adaptor were further demultiplexed by overlapping the putative Barcode to the corresponding bead barcode location file (whitelist) with an allowance of one Levenshtein edit distance. After demultiplexing, we trimmed the adaptor, bead barcode and UMI sequences for each read and wrote the reads to a new fastq file.

Immune Clonotype Data Downstream Analysis.

AIR clonotype calling and analysis. To call the TCR/BCR clonotype, we applied MiXCR (v4.6.0) (29) with a modified "generic-ont" preset that can assemble clonotypes within one mismatch or indel nucleotide in CDR3 region. The reads that did not map to any clone (cloneId = −1) or could not be aligned to the whitelist were filtered out. We then used the MiXCR output tabular file to assign reads to clonotypes and spatial bead coordination with the matched barcode. Finally, two tabular files were generated from this process: one is a metadata table for each bead barcode to display its clonotype annotation and abundance level reflected by the number of long-read UMI, which can be concatenated to the Anndata object; the other is a table containing each read along with its clonotype information and spatial barcode coordinates.

Spatial clonal evolution analysis. This analysis is mostly done using the Immcantation framework. To begin this analysis, we first assign VDJ genes using IgBLAST (28) from Immcantation Lab Docker image. Then we focused on specific IGH clones that are abundantly present in the spatial dataset by extracting relevant long-reads with custom settings. We filter out the unproductive sequences, prioritize full VDJ reads, and select the highest-quality alignment if multiple reads share the same CDR3 and barcode. The resulting data frames were merged with the metadata so that each barcode would have only one representative IGH long-read. To facilitate lineage tracing, we used "createGermlines()" function from Dowser (56) package with IMGT mouse IGH VDJ segments as reference. Observed mutation frequencies across the variable region were computed with "observedMutations()" from shazam (57) package. The lineage tree construction was done with igphyml (58), scaling branch lengths by mutation counts. The resulting trees were visualized with plotTrees(), tips were labeled and color-coded by CDR3 sequences and isotype.

Short-Read Sequencing Analysis.

Slide-seq data preprocessing for quality control and smear removal. After Illumina sequencing, the raw sequencing reads were aligned to the mouse genome (assembly: GRCm38) using the STARsolo (v2.7.10a) (59) pipeline to generate a gene x bead barcode expression count matrix. By integrating the corresponding bead barcode location files downloaded from Curio Bioscience website, slide-seq count matrix with spatial position information for each sample was generated and loaded into an AnnData object using Scanpy (v1.9.8) (60). Beads with less than 100 transcripts captured were filtered. To remove the smear effect, we also calculated the spatial distances between all pairs of beads within each sample and beads with less than 15 beads within 100 μm distance were removed.

Multilevel cell-type label assignment for spatial transcriptomics datasets. All samples of spatial transcriptomics postfiltered datasets were concatenated to a big Anndata object for performing cell-type label assignment together. First, cell2location (22) (v0.1.3) was used to deconvolve our spatial transcriptomics datasets with the combined human lymphoid organs scRNA-seq datasets as a reference same as the cell2location paper. We used a customized single-cell reference to assign cell-types as detailed in the *SI Appendix, Extended Materials and Methods*.

Region label assignment on spatial transcriptomics datasets. To identify spatially distinct regions within lymph node tissues, we employed GraphST (v0.1.3) to perform spatial domain identification. For each sample, we processed on the raw count matrices from our Slide-seq postfiltered Anndata objects with "Slide" datatype parameter to accommodate our 10-μm resolution platform. Following the model training phase, we performed spatial domain identification using Leiden clustering with an initial target of 10 clusters with refinement (method = "leiden," n _ clust = 10, increment = 0.05, refinement = True). Each resulting cluster was then manually annotated to specific lymph node anatomical structure based on the expression patterns of canonical marker genes and their spatial distribution. Taken together, the integration of spatial context with gene signatures enabled identification of key anatomical structures including the medulla, outer cortex, inner cortex (paracortex), GC, fat tissue, capsule, and conduit (interfollicular border) regions.

Identification of Ifng activation niches in the D3PI sample spatial map. To establish the *Ifng* activation niches, we first selected bins (30 μm) with high *Ifng* expression levels. The binned Anndata object from D3PI sample was performed log-normalization, regression, and scaling. Bins with *Ifng* expression levels greater than or equal to a predefined cutoff (≥4) were classified as "*Ifng*-high". The spatial coordinates of these *Ifng*-high bins were used for K-means clustering with the number of clusters set to 6. Based on their spatial location in either the Inner Cortex or Outer Cortex, they were labeled as "Inner" or "Outer," respectively. The centroids of these clusters were calculated to represent each niche. To establish "Control" niches for comparison, we identified regions with low *Ifng* expression in both cortical zones. For the inner Cortex control (Control_in), we calculated the centroid of the areas that were at least 200 μm away from the "*Ifng*-high" areas. For the Outer Cortex control (Control_out_D3 & Control_out_Mock), we computed their convex hull (scipy.spatial.ConvexHull) within the spatial extent of the outer cortex ("Capsule" and "Outer Cortex") and selected the ones away from "*Ifng*-high" areas. Beads within a 200 μm radius of each calculated centroid were assigned to their respective niche categories: "Inner," "Outer," "Control_in," "Control_out_D3," and "Control_out_Mock".

GC egress-zone analyses. Each GC was cropped within a defined grid. Within each GC crop, after removing the identified GC region, GraphST was trained and refined using Leiden clustering to identify subcompartments. Clusters were annotated as "egress_zone," "outer_cortex," or "inner_cortex" based on spatial

location and canonical gene expression patterns. Effect sizes for visualization were computed as log2 fold-change of the egress zone versus other subcompartments within the same GC, with a pseudocount of 1×10^{-4} added to avoid division by zero. Statistical comparisons between the egress zone and each other subcompartment were performed using two-sided Wilcoxon rank-sum tests. P-values were adjusted for multiple testing using the Benjamini–Hochberg method.

Data, Materials, and Software Availability. Spatial transcriptmics and long-read immune receptor sequencing data and code associated with this work have been deposited in Gene Expression Omnibus (GEO) and Github (GSE286452 (61); https://github.com/ShaowenJCornell/AIR-SPACE (62)).

ACKNOWLEDGMENTS. We thank the Cornell Biotechnology Resource Center for their help with sequencing the libraries. We thank the Cornell Center for Animal Resources and Education for animal housing and care. We thank Xander Wilcox from the Flyak lab for performing ELISA experiments to validate binding affinity. We thank Lena Takayasu, Rohit Agarwal, and other members of the De Vlaminck lab for helpful discussions and feedback.

1. M. Hirano, S. Das, P. Guo, M. D. Cooper, The evolution of adaptive immunity in vertebrates. *Adv. Immunol.* **109**, 125–157 (2011).
2. D. B. Roth, V(D)J recombination: Mechanism, errors, and fidelity. *Microbiol. Spectr.* **2**, 10.1128/microbiolspec.MDNA3-0041-2014 (2014).
3. J. M. Di Noia, M. S. Neuberger, Molecular mechanisms of antibody somatic hypermutation. *Annu. Rev. Biochem.* **76**, 1–22 (2007).
4. H. Qi, W. Kastenmüller, R. N. Germain, Spatiotemporal basis of innate and adaptive immunity in secondary lymphoid tissue. *Annu. Rev. Cell Dev. Biol.* **30**, 141–167 (2014).
5. G. V. Reynoso *et al.*, Lymph node conduits transport virions for rapid T cell activation. *Nat. Immunol.* **20**, 602–612 (2019).
6. S. M. Grant, M. Lou, L. Yao, R. N. Germain, A. J. Radtke, The lymph node at a glance–How spatial organization optimizes the immune response. *J. Cell Sci.* **133**, jcs241828 (2020).
7. W. Kastenmüller, P. Torabi-Parizi, N. Subramanian, T. Lämmermann, R. N. Germain, A spatially-organized multicellular innate immune response in lymph nodes limits systemic pathogen spread. *Cell* **150**, 1235–1248 (2012).
8. A. P. Baptista *et al.*, The chemoattractant receptor Ebi2 drives intranodal naive CD4+ T cell peripheralization to promote effective adaptive immunity. *Immunity* **50**, 1188–1201.e6 (2019).
9. M. Meyer-Hermann *et al.*, A theory of germinal center B cell selection, division, and exit. *Cell Rep.* **2**, 162–174 (2012).
10. L. Binet *et al.*, Specific pre-plasma cell states and local proliferation at the dark zone–medulla interface characterize germinal center-derived plasma cell differentiation in lymph node. bioXriv [Preprint] (2024), https://doi.org/10.1101/2024.07.26.605240. Accessed 21 October 2025.
11. Y. Zhang *et al.*, Plasma cell output from germinal centers is regulated by signals from Tfh and stromal cells. *J. Exp. Med.* **215**, 1227–1243 (2018).
12. N. J. Kräutler *et al.*, Differentiation of germinal center B cells into plasma cells is initiated by high-affinity antigen and completed by Tfh cells. *J. Exp. Med.* **214**, 1259–1267 (2017).
13. J. A. Roco *et al.*, Class-switch recombination occurs infrequently in germinal centers. *Immunity* **51**, 337–350.e7 (2019).
14. J. M. J. Tas *et al.*, Visualizing antibody affinity maturation in germinal centers. *Science* **351**, 1048–1054 (2016).
15. P. L. Ståhl *et al.*, Visualization and analysis of gene expression in tissue sections by spatial transcriptomics. *Science* **353**, 78–82 (2016).
16. R. R. Stickels *et al.*, Highly sensitive spatial transcriptomics at near-cellular resolution with Slide-seqV2. *Nat. Biotechnol.* **39**, 313–319 (2021).
17. A. Chen *et al.*, Spatiotemporal transcriptomic atlas of mouse organogenesis using DNA nanoball-patterned arrays. *Cell* **185**, 1777–1792.e21 (2022).
18. C. Engblom *et al.*, Spatial transcriptomics of B cell and T cell receptors reveals lymphocyte clonal dynamics. *Science* **382**, eadf8486 (2023).
19. S. Liu *et al.*, Spatial maps of T cell receptors and transcriptomes reveal distinct immune niches and interactions in the adaptive immune response. *Immunity* **55**, 1940–1952.e5 (2022).
20. B. D. Rudd *et al.*, Diversity of the CD8+ T cell repertoire elicited against an immunodominant epitope does not depend on the context of infection. *J. Immunol.* **184**, 2958–2965 (2010).
21. R. Volden *et al.*, Improving nanopore read accuracy with the R2C2 method enables the sequencing of highly multiplexed full-length single-cell cDNA. *Proc. Natl. Acad. Sci. U.S.A.* **115**, 9726–9731 (2018).
22. V. Kleshchevnikov *et al.*, Cell 2location maps fine-grained cell types in spatial transcriptomics. *Nat. Biotechnol.* **40**, 661–671 (2022).
23. R. Lopez *et al.*, DestVI identifies continuums of cell types in spatial transcriptomics data. *Nat. Biotechnol.* **40**, 1360–1369 (2022).
24. R. Massoni-Badosa *et al.*, An atlas of cells in the human tonsil. *Immunity* **57**, 379–399.e18 (2024).
25. Y. Long *et al.*, Spatially informed clustering, integration, and deconvolution of spatial transcriptomics with GraphST. *Nat. Commun.* **14**, 1155 (2023).
26. H. M. T. Choi *et al.*, Third-generation in situ hybridization chain reaction: Multiplexed, quantitative, sensitive, versatile, robust. *Development* **145**, dev165753 (2018).
27. D. Z. Q. Deng *et al.*, R2C2 + UMI: Combining concatemeric and unique molecular identifier–based consensus sequencing enables ultra-accurate sequencing of amplicons on Oxford Nanopore Technologies sequencers. *PNAS Nexus* **3**, pgae336 (2024).
28. J. Ye, N. Ma, T. L. Madden, J. M. Ostell, IgBLAST: An immunoglobulin variable domain sequence analysis tool. *Nucleic Acids Res.* **41**, W34–W40 (2013).
29. D. A. Bolotin *et al.*, MiXCR: Software for comprehensive adaptive immunity profiling. *Nat. Methods* **12**, 380–381 (2015).
30. B. J. DeKosky *et al.*, In-depth determination and analysis of the human paired heavy- and light-chain antibody repertoire. *Nat. Med.* **21**, 86–91 (2015).
31. C. G. Jensen, J. A. Sumner, S. H. Kleinstein, K. B. Hoehn, Inferring b cell phylogenies from paired H and L chain BCR sequences with dowser. *J. Immunol.* **212**, 1579–1588 (2024).
32. G. D. Victora, M. C. Nussenzweig, Germinal centers. *Annu. Rev. Immunol.* **40**, 413–442 (2022).
33. P. A. S. Cordeiro *et al.*, The role of IFN-γ production during retroviral infections: An important cytokine involved in chronic inflammation and pathogenesis. *Rev. Inst. Med. Trop. Sao Paulo* **64**, e64 (2022).
34. W. Kastenmüller, P. Torabi-Parizi, N. Subramanian, T. Lämmermann, R. N. Germain, A spatially-organized multicellular innate immune response in lymph nodes limits systemic pathogen spread. *Cell* **150**, 1235–1248 (2012).
35. J. Kranich *et al.*, Follicular dendritic cells control engulfment of apoptotic bodies by secreting Mfge8. *J. Exp. Med.* **205**, 1293–1302 (2008).
36. S. L. Nutt, P. D. Hodgkin, D. M. Tarlinton, L. M. Corcoran, The generation of antibody-secreting plasma cells. *Nat. Rev. Immunol.* **15**, 160–171 (2015).
37. A. Pelissier *et al.*, Convergent evolution and B-cell recirculation in germinal centers in a human lymph node. *Life Sci. Alliance* **6**, e202301959 (2023).
38. D. R. Fooksman *et al.*, Development and migration of plasma cells in the mouse lymph node. *Immunity* **33**, 118–127 (2010).
39. H. J. Sutton *et al.*, Lack of affinity signature for germinal center cells that have initiated plasma cell differentiation. *Immunity* **57**, 245–255.e5 (2024).
40. A. Sprumont, A. Rodrigues, S. J. McGowan, C. Bannard, O. Bannard, Germinal centers output clonally diverse plasma cell populations expressing high- and low-affinity antibodies. *Cell* **186**, 5486–5499.e13 (2023).
41. M. A. ElTanbouly *et al.*, Role of affinity in plasma cell development in the germinal center light zone. *J. Exp. Med.* **221**, e20231838 (2024).
42. J. Goulding *et al.*, CD8 T cells use IFN-γ to protect against the lethal effects of a respiratory poxvirus infection. *J. Immunol.* **192**, 5415–5425 (2014).
43. G. Abboud *et al.*, Natural killer cells and innate interferon gamma participate in the host defense against respiratory vaccinia virus infection. *J. Virol.* **90**, 129–141 (2016).
44. H. D. Hickman *et al.*, Direct priming of antiviral CD8+ T cells in the peripheral interfollicular region of lymph nodes. *Nat. Immunol.* **9**, 155–165 (2008).
45. I. C. MacLennan, Germinal centers. *Annu. Rev. Immunol.* **12**, 117–139 (1994).
46. C. D. C. Allen, T. Okada, J. G. Cyster, Germinal-center organization and cellular dynamics. *Immunity* **27**, 190–202 (2007).
47. L. Mesin *et al.*, Restricted clonality and limited germinal center reentry characterize memory B cell reactivation by boosting. *Cell* **180**, 92–106.e11 (2020).
48. M. Mantri *et al.*, Spatiotemporal transcriptomics reveals pathogenesis of viral myocarditis. *Nat. Cardiovasc. Res.* **1**, 946–960 (2022).
49. X. Tan *et al.*, A robust platform for integrative spatial multi-omics analysis to map immune responses to SARS-CoV-2 infection in lung tissues. *Immunology* **170**, 401–418 (2023).
50. S. Nayar *et al.*, Molecular and spatial analysis of tertiary lymphoid structures in Sjogren's syndrome. *Nat. Commun.* **16**, 5 (2025).
51. D. Zheng, T. Liwinski, E. Elinav, Interaction between microbiota and immunity in health and disease. *Cell Res.* **30**, 492–506 (2020).
52. I. Ntekas *et al.*, High resolution spatial mapping of microbiome-host interactions via in situ polyadenylation and spatial RNA sequencing. bioXriv [Preprint] (2024), https://doi.org/10.1101/2024.11.18.624127. Accessed 21 October 2025.
53. M. Meylan *et al.*, Tertiary lymphoid structures generate and propagate anti-tumor antibody-producing plasma cells in renal cell cancer. *Immunity* **55**, 527–541.e5 (2022).
54. D. W. McKellar *et al.*, Spatial mapping of the total transcriptome by in situ polyadenylation. *Nat. Biotechnol.* **41**, 513–520 (2023).
55. Y. Liu *et al.*, High-plex protein and whole transcriptome co-mapping at cellular resolution with spatial CITE-seq. *Nat. Biotechnol.* **41**, 1405–1409 (2023).
56. K. B. Hoehn, O. G. Pybus, S. H. Kleinstein, Phylogenetic analysis of migration, differentiation, and class switching in B cells. *PLoS Comput. Biol.* **18**, e1009885 (2022).
57. N. T. Gupta *et al.*, Change-O: A toolkit for analyzing large-scale B cell immunoglobulin repertoire sequencing data. *Bioinformatics* **31**, 3356–3358 (2015).
58. K. B. Hoehn, G. Lunter, O. G. Pybus, A phylogenetic codon substitution model for antibody lineages. *Genetics* **206**, 417–427 (2017).
59. B. Kaminow, D. Yunusov, A. Dobin, STARsolo: Accurate, fast and versatile mapping/quantification of single-cell and single-nucleus RNA-seq data. bioXiv [Preprint] (2021). https://doi.org/10.1101/2021.05.05.442755. Accessed 21 October 2025.
60. F. A. Wolf, P. Angerer, F. J. Theis, SCANPY: Large-scale single-cell gene expression data analysis. *Genome Biol.* **19**, 15 (2018).
61. S. Jiang *et al.*, Spatiotemporal dynamics of the lymph adaptive immune repertoire in response to viral infection. Gene Expression Omnibus. https://www.ncbi.nlm.nih.gov/geo/query/acc.cgi?acc=GSE286452. Deposited 11 January 2025.
62. S. Jiang *et al.*, AIR-SPACE code. GitHub. https://github.com/ShaowenJCornell/AIR-SPACE. Deposited 28 January 2025.